Ionics (2020) 26:913–925
https://doi.org/10.1007/s11581-019-03262-4

ORIGINAL PAPER

Fabrication of LSCF and LSCF-GDC nanocomposite thin films using polymeric precursors

Can Sındıraç[1] · Ali Ahsen[2,3] · Osman Ozturk[2,3] · Sedat Akkurt[1] · Viola I. Birss[4] · Aligul Buyukaksoy[4,5]

Received: 29 May 2019 / Revised: 15 August 2019 / Accepted: 15 September 2019 / Published online: 1 November 2019

Abstract

$La_{1-x}Sr_xCo_yFe_{1-y}O_3$ (LSCF) and LSCF-gadolinia-doped ceria (LSCF-GDC) composites are used as solid oxide fuel cell (SOFC) cathodes. In the present study, to maximize the LSCF/gas and LSCF/GDC interfacial area and thus enhance the performance, we fabricated both single-phase LSCF and composite LSCF-GDC thin-film electrodes using a facile and cost-effective polymeric precursor technique. This method involves molecular level mixing of cations in solution form and results in average particle sizes of ca. 72 nm and 60 nm upon annealing at 700 °C, respectively. For LSCF, electrochemical impedance spectroscopy measurements indicate very low electrode polarization resistances of ca. 0.6 Ω cm^2 per electrode at 600 °C. However, the addition of GDC results in poorer electrochemical activity but better microstructural and electrochemical stability, all at 600 °C. Surface analysis revealed that Fe surface segregation occurs in the single-phase LSCF, while predominantly Co segregation is observed at the LSCF-GDC composite electrode surface.

Keywords Solid oxide fuel cell · Thin-film electrodes · Impedance spectroscopy · Long-term stability · Surface composition

Introduction

The limited long-term performance and stability of solid oxide fuel cells (SOFCs) at their conventional operating temperatures of 700–800 °C hinders their viability as a viable energy conversion technology. Thus, the goal is to reduce the operating temperatures of these devices down to below 650 °C in order to avoid microstructural and chemical degradation of their components, such as microstructural coarsening in the electrodes [1, 2], surface segregation in the perovskite cathode electrocatalyst [2, 3], and oxidation of the stainless steel interconnects [4, 5].

✉ Aligul Buyukaksoy
aligul@gtu.edu.tr

[1] Department of Mechanical Engineering, Izmir Institute of Technology, Urla, 35433 İzmir, Turkey

[2] Department of Physics, Gebze Technical University, Gebze, 41400 Kocaeli, Turkey

[3] Institute of Nanotechnology, Gebze Technical University, Gebze, 41400 Kocaeli, Turkey

[4] Department of Chemistry, University of Calgary, Calgary, Alberta T2N 1N4, Canada

[5] Department of Materials Science and Engineering, Gebze Technical University, Gebze, 41400 Kocaeli, Turkey

Since oxygen reduction, fuel oxidation, and ionic transport processes that occur at the cathode, anode, and electrolyte materials, respectively, are all thermally activated processes, a decrease of the operating temperatures brings about a loss in the overall cell performance. It is now well established that, at temperatures below 650 °C, oxygen reduction at the cathode is the main contributor to the total cell resistance [6–8]. Therefore, efforts to lower the SOFC operating temperature has largely concentrated on the development of cathodes that would exhibit acceptable performance at these lowered temperatures [9–13].

The majority of the studies aiming at the development of such cathodes have been based on enhancing the electrocatalyst/gas and electrocatalyst/ionic conductor interfacial areas while using perovskite oxygen reduction electrocatalysts with mixed ionic electronic conductivity (MIEC), such as $La_{1-x}Sr_xCo_yFe_{1-y}O_3$ (LSCF) [2, 6, 8, 11]. For this purpose, LSCF has been fabricated both as a porous, single-phase layer and in the form of a composite mixed with a chemically compatible ionic conductor, e.g., gadolinia-doped ceria (GDC) [8, 13].

The most straightforward approach to producing LSCF and LSCF-GDC cathodes with high electrochemical activity at ≤ 650 °C has been to sinter suspensions containing fine powders of the corresponding phases at 850–1150 °C [14–19]. This powder-based fabrication method, in general, yielded 5–60-μm-thick cathode layers, characterized by microstructures

with average particle sizes in the 0.7–3-μm range [14, 15]. In general, sufficiently high electrochemical activities for low-temperature operation have been achieved in the case of LSCF-GDC composites prepared by the powder-based method, while relatively poor performances were observed in the case of single-phase LSCF prepared by the same route [14, 15, 18]. For example, Murray et al. reported a polarization resistance of 0.17 Ω cm^2 at 600 °C for LSCF-GDC composite cathodes, indicating a high electrochemical activity, while obtaining 2 Ω cm^2 at the same temperature in single-phase LSCF cathodes [14]. Similarly, Dusastre et al. also reported a decrease in the polarization resistance of powder-derived LSCF cathodes from 4.0 to 0.6 Ω cm^2 at 590 °C upon mixing with GDC [15].

To further enhance the LSCF/gas and LSCF/ceria interfacial area and thus facilitate oxygen adsorption and oxide ion transfer, respectively, infiltration of liquid solutions containing the cations of LSCF into previously formed porous ceria scaffolds has been studied [13, 20–25]. Upon heating the solution infiltrated porous ceria scaffold, nanoparticles of LSCF form, yielding porous LSCF-ceria composites with enhanced LSCF/air and LSCF/ceria interfacial areas [21, 26, 27]. Burye et al. reported that LSCF-GDC composites, prepared by LSCF infiltration into porous GDC scaffolds, had a microstructure consisting of LSCF particles that were ca. 48 nm in diameter with a very low polarization resistance of 0.2 Ω cm^2 at 600 °C [26]. Nie et al. reversed the process, i.e., infiltrated samarium-doped ceria (SDC) into porous LSCF scaffolds, thus lowering the polarization resistance from 1.09 to 0.44 Ω cm^2 at 600 °C [28].

The very low polarization resistances of LSCF-GDC cathodes prepared by powder sintering and infiltration methods, obtained at ≤ 650 °C, are only meaningful when they are employed in a SOFC design that, as a whole, is designed to exhibit acceptable performances at these temperatures. SOFCs consisting of thin-film electrodes and electrolytes with total thicknesses of only a few microns, i.e., micro-SOFCs, are designs that ensure short oxide ion diffusion distances both in the electrolyte and the electrodes, thus decreasing the ohmic resistances to a minimum [2, 3, 19, 29–31]. However, powder sintering and infiltration-derived LSCF-GDC cathodes are not suitable for use in micro-SOFCs, due to the high heat treatment temperatures (850–1000 °C) required in at least one of their processing steps [8]. Cathode layers in the form of thin films, on the other hand, can be fabricated by pulsed laser deposition (PLD) [32], radiofrequency (RF) magnetron sputtering [33], spray pyrolysis [34, 35], and electrostatic spray deposition (ESD) methods [36–38]. Among these studies, high polarization resistances of 8 Ω cm^2 at 750 °C and 122 Ω cm^2 at 600 °C were obtained in LSCF thin-film cathodes prepared by PLD [32] and RF magnetron sputtering [33], respectively. The main reason behind these large polarization resistances is that PLD and RF magnetron sputtering derived LSCF thin films are usually dense and thus more suitable for use in mechanistic studies as model electrodes [32, 33]. In addition, the high equipment costs associated with the PLD and RF magnetron sputtering methods are undesirable for SOFC fabrication purposes [32, 33, 39, 40].

Spray pyrolysis and ESD, on the other hand, have yielded LSCF and LSCF-GDC thin-film cathodes with nanoporous and nanoparticulate microstructures and thus lower polarization resistances [34–36]. Polarization resistances as low as 1 Ω cm^2 at 575 °C were obtained for spray pyrolysis-derived LSCF-GDC thin films [35], while the ESD process resulted in even lower polarization resistances of 0.13 Ω cm^2 at 600 °C [36]. The spray pyrolysis technique yielded LSCF-based electrode microstructures that consisted of particles with an average diameter of 124 nm [34], while the ESD-derived electrodes had a smaller average particle size of 25–50 nm [36].

In this work, as an alternative to the previously discussed methods, our goal was to fabricate single-phase LSCF and LSCF-GDC composite thin-film cathodes for SOFCs operating at ≤ 650 °C by a facile and cost-effective polymeric precursor method. Our recent efforts showed that nanoscale Ni-YSZ composite anodes fabricated by this method yielded very low polarization resistances (0.6 Ω cm^2 at 550 °C), and thus, a similar positive effect on the performance of the cathode was anticipated [30]. In this approach, polymeric precursors deposited onto dense GDC substrates by simple spin-on deposition undergo gelation instead of precipitation upon heat treatment, which results in good attachment to the substrate without the need for high-temperature annealing. In addition, this approach yields nanoscale composites as a result of the molecular level mixing, low-temperature annealing, and concurrent formation of the LSCF and GDC phases in the case of LSCF-GDC thin films.

Experimental methods

Fabrication of electrolyte substrates

Gadolinium-doped ceria powder ($Ce_{0.9}Gd_{0.1}O_3$ (GDC), PRAXAIR, > 99.9%) (10 mol %) was used for the preparation of the dense ceramic electrolyte discs. The specific surface area of the powder was 6.6 m^2/g, while the d_{10}, d_{50}, and d_{95} values were 0.4 μm, 0.6 μm, and 0.9 μm, respectively. The powder was compacted at 180 MPa pressure by uniaxial pressing (Carver Hydraulic Press, Wabash, IN, USA) in a cylindrical stainless steel die, producing pellets 15 mm in diameter and 1 mm thick. The pellets were then fired to densify in an electrically heated laboratory kiln (Nabertherm LHT 02/17, Germany) at 1400 °C for 4 h at a heating rate of 3 °C/min.

Polymeric precursor solution preparation and coating process

To deposit the LSCF thin films on the GDC electrolytes, a polymeric precursor solution that contained the stoichiometric

amounts of the constituent cations was prepared. Lanthanum(III) nitrate hexahydrate (ALFA-AESAR, > 99.99%), strontium chloride hexahydrate (ALFA-AESAR, > 99%), cobalt(II) nitrate hexahydrate (ALFA-AESAR, > 97.7% min), and iron(III) nitrate nonahydrate (ALFA-AESAR, > 99.99%) salts were dissolved in deionized water at a molar ratio that would produce the desired $La_{0.6}Sr_{0.4}Co_{0.8}Fe_{0.2}O_{3-\delta}$ (LSCF) stoichiometry. In the second step, the salt solution was mixed with ethylene glycol (ethylene glycol/cation molar ratio of 1:0.04) and stirred at 70 °C until all of the water had evaporated and polymerization took place. To lower the surface tension of the polymeric LSCF precursor and ensure good wetting of the GDC substrate upon deposition, the solution was diluted with 2-butoxyethanol (1:1 weight ratio).

For the preparation of the LSCF-GDC composite thin films, a polymeric precursor of GDC was prepared in a similar way, i.e., by adding ethylene glycol to an aqueous solution of $Gd(NO_3)_3{\cdot}6H_2O$ (Sigma-Aldrich, > 99.9%) and $Ce(NO_3)_3{\cdot}6H_2O$ (ALFA-AESAR, > 99.5%) salts and stirring at 70 °C until all of the water had evaporated and polymerization took place. Then, the polymeric precursors of LSCF and GDC were mixed in appropriate ratios to yield a volumetric LSCF/GDC ratio of 60:40. 2-Butoxyethanol was again added to the resultant solution to achieve good wetting of the GDC substrate upon deposition. Further details of the process are given elsewhere [30, 41, 42].

To produce the LSCF and LSCF-GDC thin films on the GDC electrolytes, the polymeric LSCF and LSCF-GDC precursors were deposited onto the 1-mm-thick GDC substrates by spin coating at a rotation speed of 3000 rpm (SCS G3 Spin Coater, Indianapolis, USA). The samples were then placed on a hot plate and gradually heated to 400 °C until the solvents had evaporated and the other organic constituents had decomposed, producing uniform LSCF or LSCF-GDC layers. The spin coating/decomposition cycles were repeated 30 times in order to obtain a thin film approximately 2 μm thick on the dense GDC substrates. If required, the number of spin coating/decomposition cycles to achieve the same coating thickness may be reduced simply by increasing the viscosity of the polymeric precursor of decreasing the speed of spinning. This coating process was applied on both sides of the GDC pellets to prepare symmetrical half-cells for electrochemical characterization. GDC pellets successfully coated with LSCF or LSCF-GDC were then annealed in air at 400-700 °C for various times for microstructural and structural characterization.

Figure 1 shows the temperature profile used during the electrochemical impedance spectroscopy (EIS) characterization of the thin-film electrodes. This heating/cooling protocol is divided into five stages (I–V) in order to clearly describe the thermal history of the symmetrical cells at the time of the EIS measurements.

Structural and microstructural characterization

The ability of the polymeric precursor method to form the LSCF and LSCF-GDC thin films with the desired crystal structures was determined by X-ray diffraction (XRD, Panalytical X-Pert Pro). The grazing incidence mode at an angle of θ = 1° was utilized to obtain more signal from the thin films and less from the GDC substrate. Cu Kα radiation was selected as the X-ray source.

The microstructure and thickness of the LSCF and LSCF-GDC thin films were determined by scanning electron microscopy (SEM, Philips XL 30S FEG) utilizing secondary electron (SE) imaging. More detailed microstructural/morphological analysis was carried out by atomic force microscopy (AFM, Digital Instruments-MMSPM Nanoscope IV) using the non-contact mode.

Electrochemical performance analysis

Symmetrical half-cells were prepared for electrochemical performance analysis. Au paste (Electroscience, King of Prussia, PA) was applied on top of the electrodes as the current collectors, which were contacted to Au wires connected to a Solatron ECS Modulab electrochemical analysis instrument. The electrochemical performance of the thin-film electrodes was determined by electrochemical impedance spectroscopy measurements performed at 400–700 °C, in stagnant air, using an AC excitation voltage of 20 mV. ZView software was employed to perform the fitting of the impedance data.

Surface analysis

To determine the elemental composition of the surface of the LSCF and LSCF-GDC thin-film electrodes, X-ray photoelectron spectroscopy (XPS) analyses were carried out. The analysis

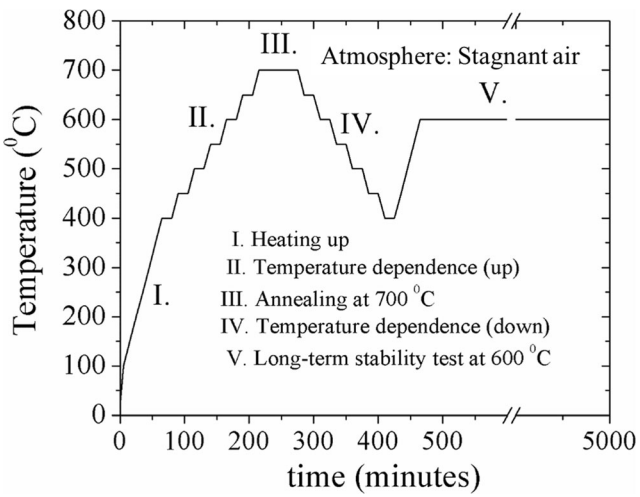

Fig. 1 Graph showing the durations for which the LSCF and LSCF-GDC electrodes were exposed to each temperature

chamber had a base pressure of 1×10^{-10} mbar and was equipped with a conventional X-ray source (Al-Kα) and Phoibos 150 Specs charged particle analyzer. The survey scan of all samples showed that each sample contained only La, Sr, Co, Fe, C, and O on the surface. In addition, the LSCF-GDC sample contained Ce and Gd. The elemental ratios of La, Sr, Co, and Fe were calculated after a detailed scan of the main peak for each element. The background signal was subtracted using a six-degree polynomial background function, while the La 3d, Sr 3d, Co 2p, and Fe 2p peaks were fitted with a Voight function.

Results and discussion

Phase analysis

In order to determine the crystal structure of the coatings, XRD studies were carried out. Glancing angle XRD patterns of the LSCF and LSCF-GDC films that were annealed either at 500 °C or at 700 °C for 2 h in air are shown in Fig. 2. A major disadvantage of the XRD analysis of LSCF thin films deposited on GDC electrolytes is that the peaks belonging to the rhombohedral LSCF (PDF:00-049-0283) and the cubic GDC (PDF:01-075-0161) overlap at 2θ = 33° 48° 58° 69° and 78°. Only the low-intensity peaks of rhombohedral LSCF at 2θ = 23°, 40.7° do not overlap with those of cubic GDC. The fact that these peaks are present in the XRD patterns of the LSCF peaks annealed at 500 and 700 °C suggests that rhombohedral LSCF is present.

The XRD patterns obtained for the LSCF thin film annealed at 500 °C show small amounts of residual phase peaks, identified as $SrCO_3$ and an unidentified peak at 36°. The presence of $SrCO_3$ during the phase evolution of LSCF has also been observed by other research groups [19, 43–46]. The peaks belonging to $SrCO_3$ are observed to disappear upon annealing at 700 °C, eventually resulting in the development of the pattern for only LSCF and GDC phases, but with only one unidentified peak remaining (Fig. 2).

The challenges associated with the overlap of the LSCF and GDC peaks are seen again and in an even more pronounced fashion in the case of LSCF-GDC composite thin films annealed at 500 and 700 °C in air (Fig. 2). This is because the LSCF content is now lower, being 60 vol% within the thin film, as opposed to the single-phase LSCF (100 vol% LSCF content), lowering the intensities of the 2θ = 23° and 40.7° peaks even further down to below the detection limit of the XRD. Angoua et al. also prepared LSCF-GDC thin films, but using spray pyrolysis of the aqueous solutions on GDC electrolytes, and reported that distinct LSCF peaks can only be seen upon heat treatment at temperatures above 800 °C [47]. They also reported that LSCF was detectable as a shoulder on the GDC peaks at 2θ = 47° upon annealing. The same shoulders are also observed in the present case of the LSCF-GDC thin films annealed at 700 °C (Fig. 2), suggesting the presence of the rhombohedral perovskite phase.

Microstructural analysis

Electrode material coated electrolyte discs were fractured down the middle to examine the cross sections and determine coating thickness, uniformity, porosity, the presence of cracks, and the degree of bonding to the substrate, using scanning electron microscopy (SEM). A representative SEM image of the LSCF-GDC nanocomposite coating, annealed at 700 °C, is shown in Fig. 3. A uniform film, adhering well to the dense substrate and with an approximate thickness of 2 μm, is observed. Some unexpectedly large pores, possibly related to the fast evaporation of organics, are also evident.

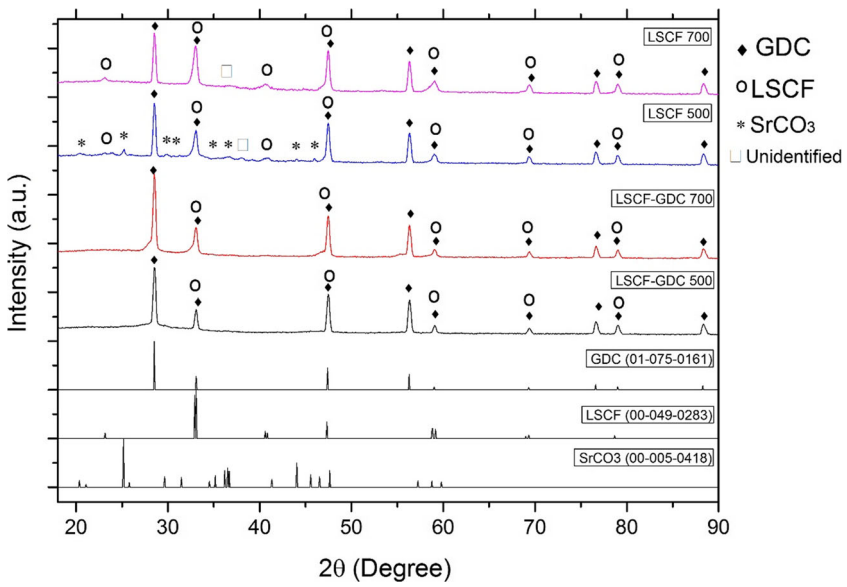

Fig. 2 X-ray diffraction patterns of LSCF and LSCF-GDC thin films, heat treated in air at 500 or 700 °C

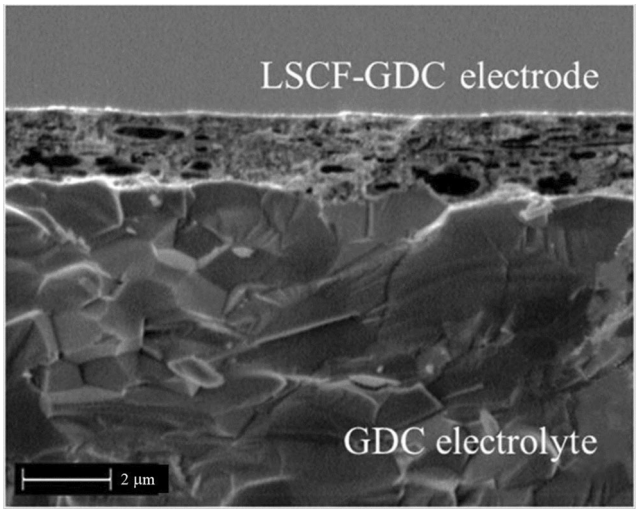

Fig. 3 A representative scanning electron microscopy image of the cross section of LSCF-GDC nanocomposite thin film deposited onto GDC electrolyte, annealed in air at 700 °C for 2 h

In order to determine the grain size and the presence of small pores, a more detailed microstructural study was performed using non-contact mode AFM. Figure 4 a–c show the AFM images of LSCF thin films annealed at 500 °C for 2 h (stage II in Fig. 1), 700 °C for 2 h (stage III in Fig. 1), and 500 °C then 600 °C for another 100 h (stage V in Fig. 1). A uniform grain size of ca. 45 nm is observed in the LSCF thin films annealed at 500 °C for 2 h (Fig. 4a). Upon annealing at 700 °C for 2 h, the grain size is seen to have increased to ca. 72 nm, with same nanoporosity of even smaller size becoming apparent (Fig. 4b). This particle size is ca. 10% of that reported in the literature for LSCF-based air electrodes, fabricated by the sintering of powders [15].

In order to assess the microstructural stability upon long-term operation at intermediate operating temperatures, the thin films were annealed at 600 °C for 100 h after being exposed to 700 °C for 2 h. In this case, further grain growth to ca. 83 nm is observed by AFM analysis of the single-phase LSCF thin films (Fig. 4c). On the other hand, the LSCF-GDC coated samples showed almost no change in their average grain size, remaining at ca. 60 nm after being exposed to the same heat treatment conditions (Fig. 4d–f). The addition of GDC, with its high sintering temperature, to the LSCF phase appears to impede grain growth, resulting in very promising morphological stability. This feature, in turn, is expected to induce electrochemical stability as well.

Electrochemical analysis

EIS analysis of the symmetrical LSCF/GDC/LSCF and LSCF-GDC/GDC/LSCF-GDC cells was performed in air. As-deposited thin films were exposed to the heating regime shown in Fig. 1, and EIS measurements were obtained at each step in stage IV and intermittently in stage V.

Representative EIS spectra, obtained from symmetrical cells with single-phase LSCF and nanocomposite LSCF-GDC thin-film electrodes at the open circuit potential (OCP), all at 600 °C and in stagnant air, are shown in Fig. 5. For the fitting and interpretation of the EIS data, a Gerischer element, connected in series with a resistor, was used initially, but good fittings could not be achieved. Therefore, an

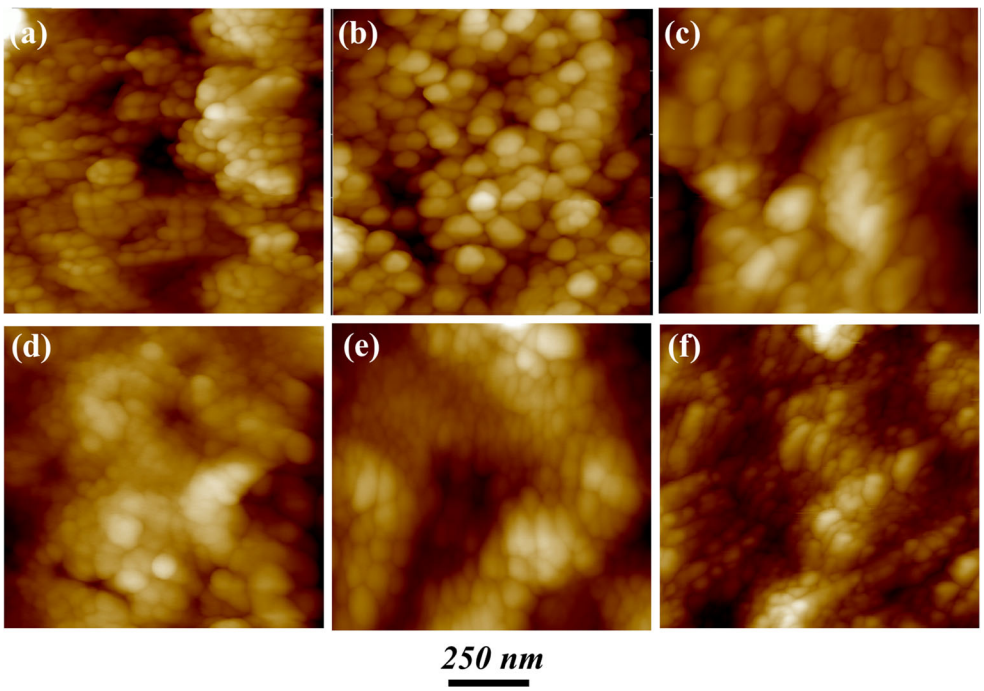

Fig. 4 Atomic force microscopy (AFM) images of single-phase LSCF, annealed at **a** 500 °C, **b** 700 °C for 2 h, and **c** at 600 °C for 80 h following the prior heat treatments. The bottom row shows the AFM images of LSCF-GDC composite thin films, also annealed at **d** 500 °C, **e** 700 °C for 2 h, and **f** at 600 °C for 80 h using the same heat treatments

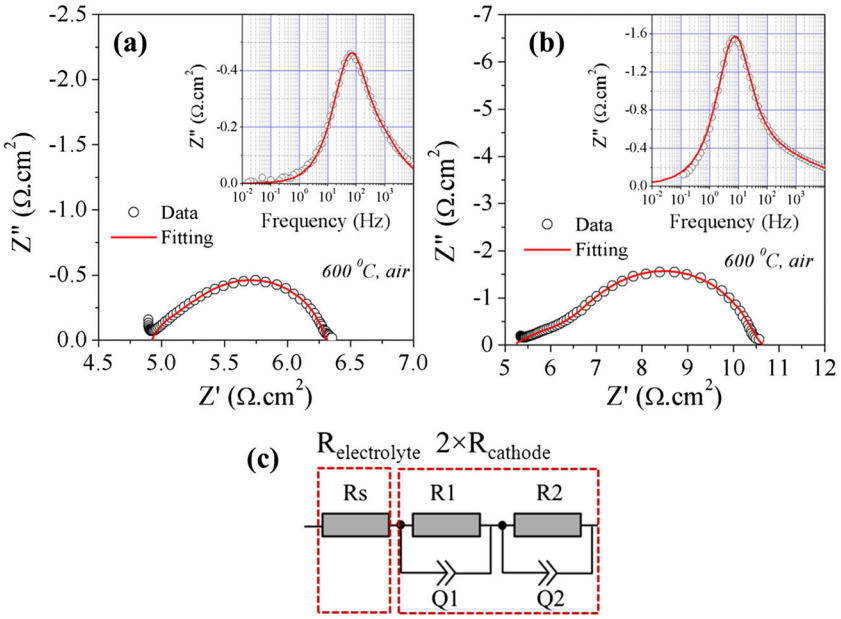

Fig. 5 Impedance spectra obtained from **a** LSCF/GDC/LSCF and **b** LSCF-GDC/GDC/LSCF-GDC symmetrical half-cells at 600 °C, in air, **c** the equivalent circuit model used to fit the obtained impedance data

equivalent circuit model, consisting of a series resistance (R_s) in series with two time constants (resistor in parallel to a constant phase element), coded as (R_1Q_1) and (R_2Q_2), was used for the EIS fitting. Since a symmetrical cell configuration was used here, R_1+R_2 corresponds to the total polarization resistance of the two electrodes, with the area specific resistance (ASR) of each electrode given by (R/2) × area.

For both the LSCF and LSCF-GDC thin films, a very good fit to this equivalent circuit was achieved ($\chi^2 \sim 10^{-4}$), allowing the accurate determination of the ASR for each electrode. However, because the two time constants are very similar, it was not possible to accurately determine the R_1 and R_2 values separately. In previous work by Molero-Sanchez et al., the EIS responses of the mixed conductor, $La_{0.3}$(Sr or Ca)$_{0.7}Fe_{0.7}Cr_{0.3}O_{3-\delta}$ (LSFCr or LCFCr), have been studied in detail to elucidate the oxygen reduction/evolution mechanisms [48, 49]. In agreement with the present results, the EIS spectra consisted of two semicircles, but with time constants that were further apart from each other, which facilitated the determination of the respective resistance and capacitance values for the LMFCr case (M=Sr, Ca) [48, 49]. In their work, the high-frequency semicircle of the EIS response was ascribed to oxide ion transfer at the mixed conductor/ionic conductor interface, while the low-frequency semicircle was related to oxygen adsorption/desorption, combined with electron transfer, at the mixed conductor/air interface [48, 49]. Although not clearly distinguishable in the Nyquist and Bode plots shown in Fig. 5, it is likely that the EIS responses of the LSCF and LSCF-GDC thin-film electrodes, prepared here by the polymeric precursor method, also consists of these two processes.

At 600 °C, the R_s values (Fig. 5) are 4.8 and 5.4 Ω cm^2 for the LSCF and LSCF-GDC thin-film electrodes, respectively. These values are in the range of what is expected for a ca. 1-mm-thick GDC electrolyte (the electrical conductivity of GDC is ca. 0.025 S/cm at 600 °C [50]), with the slight differences likely due to small variations in the GDC pellet thickness. Interestingly, the single-phase LSCF shows a lower ASR value of 0.72 Ω cm^2 at 600 °C than that exhibited by LSCF-GDC (2.8 Ω cm^2) at the same temperature (Fig. 5).

In order to determine whether this trend persists over a wider temperature range and to obtain more information about the ORR/OER mechanism, EIS measurements were performed at 400–700 °C and the ASR values for each electrode were plotted versus 1000/T (Fig. 6). Figure 6 also provides a comparison with data from the literature for thick and thin LSCF and LSCF-GDC films fabricated by other methods [14, 16, 28, 32–36]. The activation energies associated with the $ASR_{electrode}$ of the electrode materials under investigation here (Fig. 6) were determined from the Arrhenius equation (Eq. 1):

$$ASR_{electrode} = A \exp\left(\frac{Ea}{kT}\right) \quad (1)$$

where A is the pre-exponential factor, Ea is the activation energy, k is the Boltzman constant, and T is the absolute temperature.

In general, the LSCF thin films prepared by the polymeric precursor technique yield a very low $ASR_{electrode}$ value and an Ea of 1.40 eV, which is within the generally observed range of 1.19–1.63 eV (Fig. 6). In comparison to the single-phase LSCF electrodes, which have thicknesses varying between 20 and 60 μm and were fabricated by powder sintering methods, those prepared here in the form of ca. 2-μm-thick films using the polymeric precursor method gave much lower $ASR_{electrode}$ values (Fig. 6). For example, the lowest

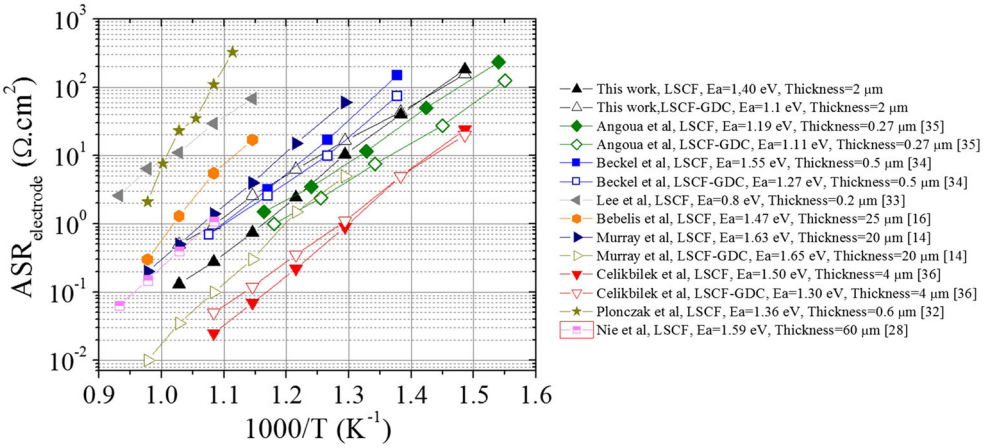

Fig. 6 Impedance spectra obtained from the temperature dependence of the polarization resistance ($ASR_{cathode}$) values obtained from the fitting of the impedance data. The polarization resistance data, obtained other groups are included for comparison

$ASR_{electrode}$ value reported for the sintered LSCF electrodes is ca. 1.5 Ω cm^2 at 600 °C, corresponding to ca. five times that obtained in the present work (Fig. 6). This difference is likely due to the nanoscale electrode morphology reported here, as opposed to the micron-sized features of the electrodes produced by powder sintering methods [32–35].

The LSCF thin films fabricated by the polymeric precursor method in this work also significantly outperform those prepared by PLD and RF magnetron sputtered methods, due to the lack of porosity reported in those studies [32, 33], as opposed to the microscale (Fig. 3) and nanoscale porosity (Fig. 4) observed here. Angoua et al. [35] and Beckel et al. [34] fabricated LSCF films with thicknesses of 0.27 and 0.5 µm, respectively, both by spray pyrolysis. Similar microstructures, having grain sizes of the order of ca. 70 nm, were obtained for the spray pyrolysis derived cathodes [34, 35] and those reported here, prepared by the polymeric precursor technique. However, the electrode polarization resistances of the polymeric precursor derived LSCF thin films are somewhat lower at temperatures above 500 °C.

The lowest $ASR_{electrode}$ values reported for the single-phase LSCF electrodes are those fabricated by ESD with a thickness of ca. 4 µm (Fig. 6) [36]. These electrodes are also the only ones that exceed the electrochemical activity of the LSCF thin films reported here (Fig. 6). These promising performances were achieved as a result of optimized microstructures (e.g., pore size distribution) and electrode thicknesses for the given morphology. For example, an earlier report by the same group [37] indicates an $ASR_{electrode}$ of 1.2 Ω cm^2 in the case of 13-µm-thick LSCF before achieving the maximum performances given in Fig. 6. Considering this, it is suggested that there is potential for improvement in the initial electrode performance of the LSCF thin films prepared by the polymeric precursor technique, reported for the first time here.

The LSCF-GDC thin films, prepared by the polymeric precursor technique, yield higher $ASR_{electrode}$ values than the single-phase LSCF, prepared by the same method over the 500–700 °C range (Fig. 6). These $ASR_{electrode}$ values are in the range of those reported by Beckel et al. for spray pyrolysis derived LSCF-GDC thin films [34].

This decrease in performance upon the addition of the GDC phase is accompanied by a decrease in the *Ea* from 1.40 to 1.10 eV (Fig. 6). The general trend in the literature, as seen in Fig. 6, is a decrease in the activation energy, concomitant with a decrease in the $ASR_{electrode}$ values. The reason for the decrease in *Ea* accompanied by an increase in $ASR_{electrode}$ is explained

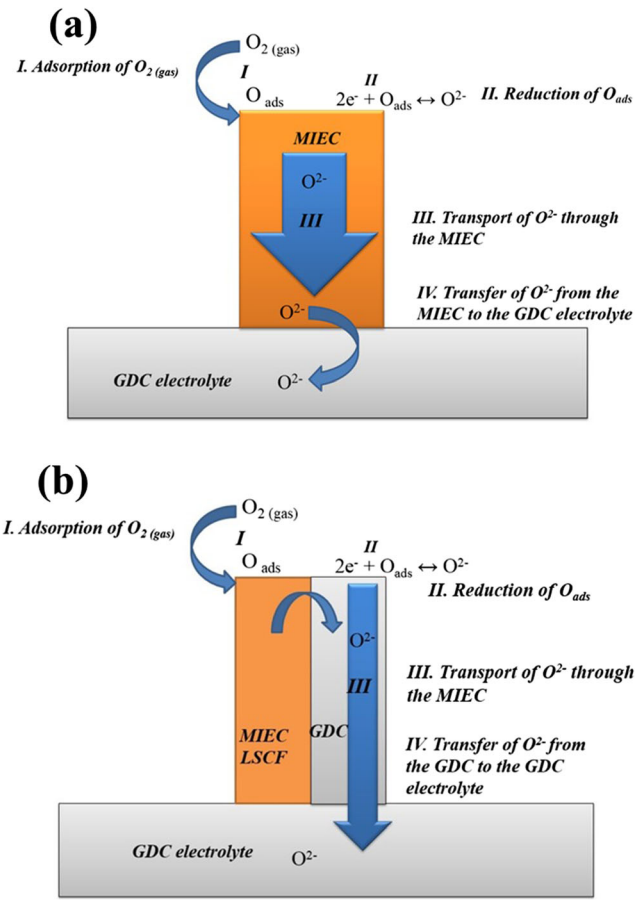

Fig. 7 Schematic representation of the proposed oxygen pathways for **a** single-phase LSCF and **b** LSCF-GDC nanocomposite cathode

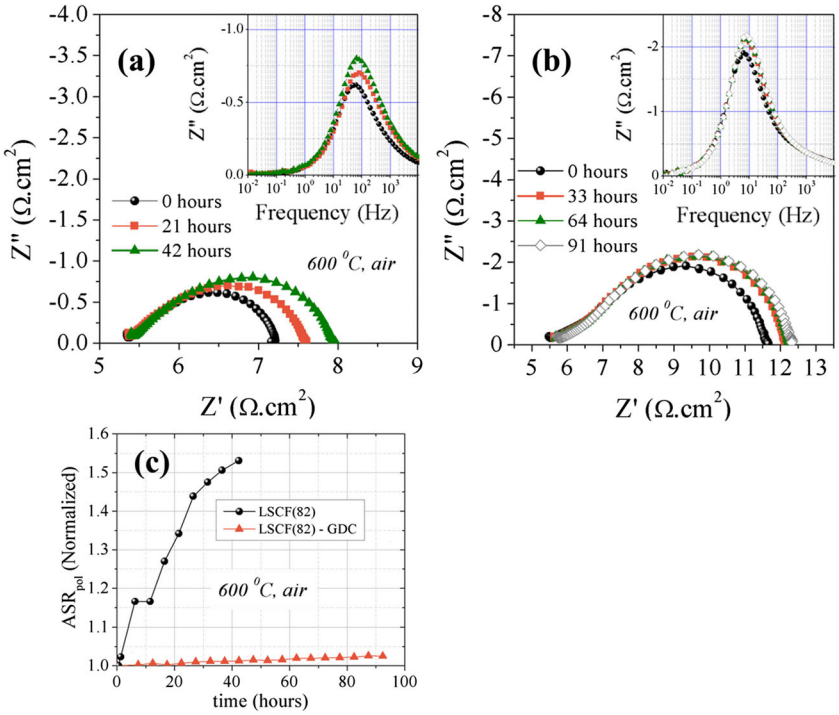

Fig. 8 Changes in the impedance spectra obtained from **a** symmetrical LSCF/GDC/LSCF half-cells, **b** symmetrical LSCF-GDC/GDC/LSCF-GDC half-cells, and **c** the normalized polarization resistances of both the LSCF and LSCF-GDC thin-film electrodes with time at 600 °C

schematically in Fig. 7, which shows what are likely the main steps during oxygen reduction (ORR) and vice versa (in the reverse direction) during oxygen evolution (OER), with both processes being relevant during EIS measurements carried out at the OCP. It is generally accepted that, during the ORR at LSCF electrodes, oxygen is initially adsorbed on the LSCF surface (step I), followed by its reduction to O^{2-}. While this reduction reaction likely consists of many individual steps, these are not generally apparent as separate time constants in EIS studies at LSCF. The O^{2-} ions are then transported (step II) through the LSCF lattice due to its mixed ionic-electronic conducting properties (MIEC) (step III). Finally, the O^{2-} ion transfer from the electrode into the electrolyte (step IV) (Fig. 7a).

In Fig. 7b, the addition of GDC to LSCF is shown to provide multiple other pathways during the ORR. Specifically, instead of the sluggish transport through the LSCF phase, which is known to be an order of magnitude lower in its ionic conductivity compared to the electrolyte material (GDC) [14, 15], O^{2-} ions likely prefer to diffuse through the GDC phase, which offers much less resistance to diffusion and thus would require a smaller activation energy (Fig. 7) than does O^{2-} transport through LSCF [14, 15]. Hence, the overall activation energy is lowered in the case of the composite catalyst.

In this scheme, if the rate limiting step is oxygen exchange at the surface rather than oxygen ion transport in the LSCF lattice, although the addition of GDC may induce some reduction in *Ea*, it may also cause an increase in $ASR_{electrode}$ due to the LSCF/gas interfacial area lost as a result of the partial replacement of LSCF by GDC (Fig. 7). Due to their relatively small thickness (ca. 2 μm) and their Co-rich compositions providing high ionic conductivity, the rate limiting step is oxygen exchange at the surface of the LSCF films fabricated here and thus the scenario mentioned above holds. Celikbilek et al. [36] also observed a decrease in *Ea* without a decrease in the $ASR_{electrode}$ value, but attributed this to a change in porosity of the electrode layer induced by GDC addition. Here, we observe no such effect (Fig. 4).

Long-term stability tests

The long-term stability of the polymeric precursor-derived LSCF and LSCF-GDC thin films was evaluated by intermittently collecting EIS data at 600 °C in stagnant air. The long-term stability test corresponds to stage V in the heating regime given in Fig. 1. This means that, prior to these tests, the samples were heated to 400 °C (stage I), then stepwise up to 700 °C (stage II), annealed at this temperature for 2 h (stage III), and finally cooled down to 400 °C (stage IV) stepwise. A comparison of the changes in the impedance spectra of the LSCF and LSCF-GDC thin-film catalysts with time at 600 °C is given in Fig. 8 a and b. The total polarization resistance increased from ca. 2 to 2.7 Ω cm^2 in 42 h at 600 °C in stagnant air in the case of the single phase LSCF thin film (Fig. 8a). On the other hand, a much smaller increase is observed in the case of the LSCF-GDC nanocomposite thin films under the same conditions (increasing from 6.3 to only 6.7 Ω cm^2 in 91 h in

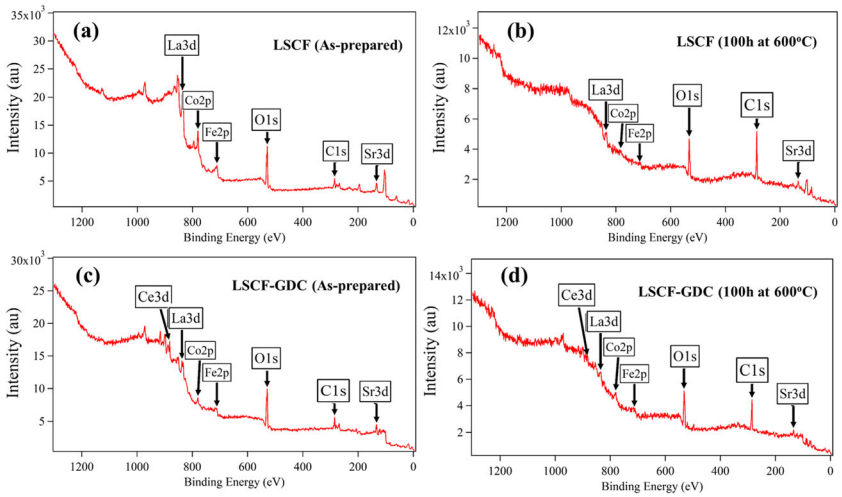

Fig. 9 X-ray photoelectron spectroscopy survey scans of LSCF thin films **a** prior to and **b** after long-term annealing at 600 °C, in stagnant air, LSCF-GDC thin films **c** prior to and **d** after long-term annealing at 600 °C, in stagnant air

air). For a clearer comparison, the polarization resistances of both of these electrodes were normalized to their values at the beginning of the long-term measurement and are plotted against time in Fig. 8c. The ASR value of the single-phase LSCF thin film increased by 54% in 42 h in air, while the LSCF-GDC nanocomposite thin film exhibited a much more stable electrochemical performance, showing an increase of only 7% in the ASR value over the same time period.

An important parameter that can be detrimental in terms of the long-term performance of thin-film electrodes for SOFC applications is their microstructural stability. As discussed earlier, the single-phase LSCF thin film exhibits a noticeable microstructural coarsening upon long-term annealing at elevated temperatures (Fig. 4a–c), likely causing the electrochemically active surface area to diminish. On the other hand, the LSCF-GDC composite thin films exhibit a stable microstructure upon annealing (Fig. 4d–f), correlated with the retention of its electrochemically active surface area, and thus its ASR value.

Despite the clear correlation observed here between the microstructural and electrochemical stability of the LSCF and LSCF-GDC electrodes, we cannot rule out changes in surface chemistry and their effect on the electrochemical performance. It has been asserted in recent reports that the segregation of various species at the surface of oxide electrodes upon long-term operation in air could have detrimental effects on the stability of their electrochemical performance [15, 51, 52].

In order to determine if there were any changes in the surface chemistry of the LSCF and LSCF-GDC thin-film electrodes upon long-term operation at 600 °C, XPS analyses were performed. The analyses were carried out before and after operation at 600 °C, i.e., at the beginning and end of stage V of the heating protocol shown earlier in Fig. 1. The corresponding survey scans provided in Fig. 9 indicate the presence of La, Sr, Co, Fe, and O, as well as some carbon at the surface of the LSCF thin films prior to and after long-term annealing at 600 °C. In the case of LSCF-GDC thin films, peaks corresponding to Ce are also apparent. The survey scans also show that the signal intensities from both the LSCF and LSCF-GDC thin films decrease after long term annealing. Therefore, the detailed analysis for each element was performed using a low scan rate (0.1 eV steps) to increase the resolution.

The relative amounts of the cations at the LSCF perovskite surface were calculated from the areas of the relevant XPS peaks of the cations. Table 1 provides a summary of the surface composition of the LSCF and LSCF-GDC thin-film materials before and after long-term exposure to 600 °C. The polymeric precursors used for the preparation of the LSCF phases in both the single phase and composite thin films had a cation ratio of La:Sr:Fe:Co = 30:20:10:40, which should equate to the cation ratios in the bulk of the films. Before annealing in air at 600 °C (at the beginning of stage V), Table 1 shows that the surface of the LSCF thin films appears to contain much more Fe and much less Co than in the bulk. Upon annealing at 600 °C for 100 h in air, the surface of the LSCF becomes even richer in Fe and slightly poorer in Co, i.e., the Fe content increases from 28 to 44%, while the Co content decreases from 21 to 17% (Table 1). In addition, prior to long-term annealing, the La content at the LSCF surface is 35%, which is slightly higher than in the bulk. Upon long-term annealing at 600 °C, the La content decreases to ca. 20% at the surface. On the other hand, the Sr content is close to that expected for the bulk of the material, both before and after long-term annealing.

In the case of the LSCF-GDC nanocomposite thin films, the surface is observed to contain 33% Sr and 27% Fe at short times, while in the bulk of the LSCF-GDC film, the LSCF phase should consist of 20% Sr and 10% Fe (Table 1). This

Table 1 Surface cation % of LSCF and LSCF-GDC thin films, annealed at 700 °C for 2 h, before and after long-term annealing at 600 °C, obtained from X-ray photoelectron spectroscopy analyses

	Atomic % of each element present according to XPS results			
	La	Sr	Fe	Co
Bulk	30	20	10	40
LSCF before long-term annealing at 600 °C	35.1	16.2	27.6	21.0
LSCF after long-term annealing at 600 °C	19.6	19.4	43.9	17.1
LSCF-GDC before long-term annealing at 600 °C	26.9	32.8	27.2	13.1
LSCF-GDC after long-term annealing at 600 °C	18.6	9.3	20.6	51.6

points to the preferential segregation of these elements at the surface. Long-term annealing at 600 °C causes a decrease in the relative amounts of La (from 26.9 to 18.6%), Sr (from 32.8 to 9.3%), and Fe (from 27.2 to 20.6 %), but an increase (from 13.1 to 51.6 %) in Co at the LSCF/air interface, pointing to Co enrichment at the surface.

A-site segregation is commonly observed at the surface of oxide perovskites, where Sr is the A-site dopant and La is the A-site host. For example, Lee et al. observed that the surface of $La_{0.8}Sr_{0.2}MnO_3$ (LSM) thin films, fabricated by PLD, became rich in SrO particles upon being annealed at 800 °C for 1 h in air [53]. Very similar results were also obtained for PLD-derived $La_{0.6}Sr_{0.4}CoO_3$ thin films upon annealing at 650 °C in air [54]. The reason for the segregation phenomenon is due to two driving forces, the first being the elastic strain generated by the size mismatch between the larger Sr (dopant) and the La (host), causing Sr to be expelled from the lattice. A second driver is the electrostatic interactions between the negatively charged Sr'_{La} and the positively charged oxygen vacancies $V_{\ddot{O}}$ that are mostly concentrated at the perovskite surface [55].

It should be noted that detailed investigations of surface segregation on oxide perovskite surfaces has been performed on thin films fabricated by pulsed laser deposition [53–55], while several studies have also examined perovskites prepared by liquid precursor based methods [23, 56]. In this case, contrary to what has been reported for PLD-derived thin-film perovskites, B-site surface segregation takes place at the electrode surface, instead of A-site segregation [23]. For example, Dieterle et al. observed the formation of Co_3O_4 precipitates in $La_{0.6}Sr_{0.4}CoO_3$ thin-film perovskites prepared by a propionic acid-based precursor method upon long-term annealing in air at 700 and 800 °C [57].

B-site enrichment at the LSCF and LSCF-GDC nanocomposite thin-film surfaces observed here is similar to what has been reported for liquid precursor derived perovskite materials in the literature [56]. In the LSCF sample, Fig. 9 and Table 1 show that Fe enrichment is observed after long-term heat treatment. In the case of the LSCF-GDC thin films, although the surface was rich in Sr and Fe initially, Co enrichment occurs upon long-term annealing. It should also be noted that, at the LSCF-GDC surface, the relative amount of Fe (20.6%) is still higher than the expected bulk value (10%) after long-term annealing, but much less pronounced in comparison to the case of long-term annealed LSCF. The reason for the different B-site cation (Fe or Co) segregation in the absence and presence of the GDC phase upon long-term annealing is likely that Fe tends to dissolve in GDC [58, 59], which could have prevented its segregation to the outer surface, allowing Co to take its place.

Overall, these results show that the addition of GDC to LSCF thin-film cathodes influences the evolution of both the microstructure and the surface composition. The fact that the stabilization of the electrochemical performance at 600 °C is concomitant with the stabilization of the microstructural features (e.g., grain size) upon GDC addition to LSCF points to a strong correlation between these two parameters. Our XPS analyses suggest that the surface composition is dynamic, rather than stable, during exposure to air at 600 °C for both the LSCF and LSCF-GDC thin films. This is because the addition of GDC to the LSCF appears to suppress Fe segregation at the LSCF/air interface. However, the fact that Co segregates to the air/LSCF interface makes it difficult to rule out the evolution of the surface chemistry as relevant to the long-term stability of the LSCF and LSCF-GDC thin-film electrodes under study here.

Summary

In this work, our goal was to fabricate single-phase $La_{1-x}Sr_xCo_{1-y}Fe_yO_3$ (LSCF) and composite LSCF-gadolinia-doped ceria (GDC) thin-film electrodes for use as cathodes in intermediate temperature solid oxide fuel cell (IT-SOFC) applications by using a facile and cost-effective polymeric precursor method to obtain nanoscale morphology and thus low polarization resistances in air at 600 °C. The microstructure of the LSCF thin films annealed at 700 °C consisted of particles of 72-nm average size, which increased to 83 nm upon long-term annealing at 600 °C, thus retaining their nanosizes. The LSCF-GDC composite electrodes exhibited microstructures with average particle sizes of ca. 60 nm, which remained significantly more stable upon long-term annealing at 600 °C.

The electrochemical performance of the LSCF and LSCF-GDC thin-film electrodes was evaluated by electrochemical impedance spectroscopy (EIS) measurements carried out at the open circuit potential in air using symmetrical half-cells. Electrode polarization resistances of 0.72 Ω cm^2 and 2.75 Ω cm^2 (per electrode) were achieved in single-phase LSCF and LSCF-GDC composite at 600 °C in stagnant air, respectively. This contradicts with most of the previous results in the

literature, which have reported an increase in the electrochemical activity upon the addition of an ionic conductor to the LSCF perovskite.

This contradiction was explained here by the fact that the Co-rich composition of the LSCF studied in the present case exhibits high enough ionic conductivity that the introduction of another ionically conductive (but electrocatalytically inactive) phase is not necessary. Therefore, the partial replacement of the electrocatalytic LSCF that also exhibits ionic conductivity results primarily in a loss of electrocatalytically active LSCF surface area.

The longevity tests revealed that, at 600 °C, the single-phase LSCF thin film exhibited a ca. 50% increase in polarization resistance in 40 h, whereas the LSCF-GDC thin film remained very stable, showing only a ca. 3% increase. This difference between the long-term performances of the single phase and composite electrode materials was found to be related to the differences in the evolution of their microstructure and possibly also their surface chemistry. X-ray photoelectron spectroscopy analyses showed that Fe and Fe/Co enrichment occurs at the outer surface of the single-phase LSCF and composite LSCF-GDC thin films, respectively, upon prolonged exposure to 600 °C in air, which may also have some impact on the long-term stability of these two types of electrodes. The B-site segregation observed here, as opposed to the findings in the literature that suggested the occurrence of Sr surface enrichment in similar materials, is likely due to differences in the thin film fabrication techniques used.

In conclusion, the fact that the polymeric precursor derived LSCF exhibits similar (and at certain temperatures, still lower) polarization resistances to those reported by others for spray pyrolysis derived LSCF thin-film electrodes suggests that this cost-effective and facile technique can be adopted for thin film SOFC electrode fabrication. However, the addition of GDC, while useful for microstructural stabilization, must be kept to a minimum in order to ensure that not too much of the catalytically active LSCF surface is sacrificed.

Acknowledgements The authors also thank the Natural Sciences and Engineering Research Council of Canada (NSERC) and the Izmir Institute of Technology for the overall support of this research. Thanks are also due to Dr. Orhan Ozturk for his help with the XRD measurements.

Funding information AB is financially supported by the Eyes High PDF program at the University of Calgary and Alberta Innovates – Technology Futures (AITF). This project was also partially supported by the Izmir Institute of Technology (BAP project number: 2015IYTE31).

References

1. Huijsmans J, Berkel FV, Christie G (1998) Intermediate temperature SOFC – a promise for the 21st century. J Power Sources 71: 107–110. https://doi.org/10.1016/s0378-7753(97)02789-4
2. Tarancón A (2009) Strategies for lowering solid oxide fuel cells operating temperature. Energies 2:1130–1150. https://doi.org/10.3390/en20401130
3. Barnett S (1990) A new solid oxide fuel cell design based on thin film electrolytes. Energy 15:1–9. https://doi.org/10.1016/0360-5442(90)90059-b
4. Weber A, Ivers-Tiffée E (2004) Materials and concepts for solid oxide fuel cells (SOFCs) in stationary and mobile applications. J Power Sources 127:273–283. https://doi.org/10.1016/j.jpowsour.2003.09.024
5. Stambouli AB, Traversa E (2002) Fuel cells, an alternative to standard sources of energy. Renew Sust Energ Rev 6:295–304. https://doi.org/10.1016/s1364-0321(01)00015-6
6. Adler SB (2004) Factors governing oxygen reduction in solid oxide fuel cell cathodes. Chem Rev 104:4791–4844. https://doi.org/10.1021/cr020724o
7. Chen C, Bouwmeester HJM, Kruidhof H, Elshof JET, Burggraaf AJ (1996) Fabrication of La1 –xSrxCoO3 –δthin layers on porous supports by a polymeric sol–gel process. J Mater Chem 6:815–819. https://doi.org/10.1039/jm9960600815
8. Beckel D, Bieberle-Hütter A, Harvey A, Infortuna A, Muecke U, Prestat M, Rupp J, Gauckler L (2007) Thin films for micro solid oxide fuel cells. J Power Sources 173:325–345. https://doi.org/10.1016/j.jpowsour.2007.04.070
9. Kharton V, Marques F, Atkinson A (2004) Transport properties of solid oxide electrolyte ceramics: a brief review. Solid State Ionics 174:135–149. https://doi.org/10.1016/j.ssi.2004.06.015
10. Nielsen J, Jacobsen T, Wandel M (2011) Impedance of porous IT-SOFC LSCF:CGO composite cathodes. Electrochim Acta 56: 7963–7974. https://doi.org/10.1016/j.electacta.2011.05.042
11. Bieberle-Hütter A, Beckel D, Infortuna A, Muecke UP, Rupp JL, Gauckler LJ, Rey-Mermet S, Muralt P, Bieri NR, Hotz N, Stutz MJ, Poulikakos D, Heeb P, Müller P, Bernard A, Gmür R, Hocker T (2008) A micro-solid oxide fuel cell system as battery replacement. J Power Sources 177:123–130. https://doi.org/10.1016/j.jpowsour.2007.10.092
12. Vohs JM, Gorte RJ (2009) High-Performance SOFC Cathodes Prepared by Infiltration. Adv Mater 21:943–956. https://doi.org/10.1002/adma.200802428
13. Jiang SP (2012) Nanoscale and nano-structured electrodes of solid oxide fuel cells by infiltration: Advances and challenges. Int J Hydrog Energy 37:449–470. https://doi.org/10.1016/j.ijhydene.2011.09.067
14. Murray EP, Sever MJ, Barnett SA (2002) Electrochemical performance of (La,Sr)(Co,Fe)O_3–(Ce,Gd)O_2 composite cathodes. Solid State Ionics 148:27–34. doi: https://doi.org/10.1016/s0167-2738(02)00102-9
15. Dusastre V, Kilner J (1999) Optimisation of composite cathodes for intermediate temperature SOFC applications. Solid State Ionics 126:163–174. https://doi.org/10.1016/s0167-2738(99)00108-3
16. Bebelis S, Kotsionopoulos N, Mai A, Tietz F (2006) Electrochemical characterization of perovskite-based SOFC cathodes. J Appl Electrochem 37:15–20. https://doi.org/10.1007/s10800-006-9215-y
17. Liu M, Ding D, Blinn K, Li X, Nie L, Liu M (2012) Enhanced performance of LSCF cathode through surface modification. Int J Hydrog Energy 37:8613–8620. https://doi.org/10.1016/j.ijhydene.2012.02.139
18. Wang W, Mogensen M (2005) High-performance lanthanum-ferrite-based cathode for SOFC. Solid State Ionics 176:457–462. https://doi.org/10.1016/j.ssi.2004.09.007
19. Leng Y, Chan S, Liu Q (2008) Development of LSCF–GDC composite cathodes for low-temperature solid oxide fuel cells with thin film GDC electrolyte. Int J Hydrog Energy 33:3808–3817. https://doi.org/10.1016/j.ijhydene.2008.04.034

20. Tomov RI, Mitchell-Williams T, Gao C, Kumar RV, Glowacki BA (2017) Performance optimization of LSCF/Gd:CeO2 composite cathodes via single-step inkjet printing infiltration. J Appl Electrochem 47:641–651. https://doi.org/10.1007/s10800-017-1066-1
21. Chrzan A, Karczewski J, Gazda M, Szymczewska D, Jasinski P (2017) La 0.6 Sr 0.4 Co 0.2 Fe 0.8 O 3-δ oxygen electrodes for solid oxide cells prepared by polymer precursor and nitrates solution infiltration into gadolinium doped ceria backbone. J Eur Ceram Soc 37:3559–3564. https://doi.org/10.1016/j.jeurceramsoc.2017.04.032
22. Shah M, Barnett S (2008) Solid oxide fuel cell cathodes by infiltration of La0.6Sr0.4Co0.2Fe0.8O3−δ into Gd-doped ceria. Solid State Ionics 179:2059–2064. https://doi.org/10.1016/j.ssi.2008.07.002
23. Liu Y, Wang F, Chi B, Pu J, Jian L, Jiang SP (2013) A stability study of impregnated LSCF–GDC composite cathodes of solid oxide fuel cells. J Alloys Compd 578:37–43. https://doi.org/10.1016/j.jallcom.2013.05.021
24. Shah M, Voorhees PW, Barnett SA (2011) Time-dependent performance changes in LSCF-infiltrated SOFC cathodes: The role of nano-particle coarsening. Solid State Ionics 187:64–67. https://doi.org/10.1016/j.ssi.2011.02.003
25. Kim JH, Kim H (2012) Ce0.9Gd0.1O1.95 supported La0.6Sr0.4Co0.2Fe0.8O3−δ cathodes for solid oxide fuel cells. Ceram Int 38:4669–4675. https://doi.org/10.1016/j.ceramint.2012.02.049
26. Burye TE, Nicholas JD (2015) Improving La 0.6 Sr 0.4 Co 0.8 Fe 0.2 O 3−δ infiltrated solid oxide fuel cell cathode performance through precursor solution desiccation. J Power Sources 276:54–61. https://doi.org/10.1016/j.jpowsour.2014.11.082
27. Burye TE, Nicholas JD (2016) Precursor solution additives improve desiccated $La_{0.6}Sr_{0.4}Co_{0.8}Fe_{0.2}O_{3-x}$ infiltrated solid oxide fuel cell cathode performance. J Power Sources 301:287–298. https://doi.org/10.1016/j.jpowsour.2015.10.012
28. Nie L, Liu M, Zhang Y, Liu M (2010) $La_{0.6}Sr_{0.4}Co_{0.2}Fe_{0.8}O_{3-\delta}$ cathodes infiltrated with samarium-doped cerium oxide for solid oxide fuel cells. J Power Sources 195:4704–4708. https://doi.org/10.1016/j.jpowsour.2010.02.049
29. Gauckler LJ, Beckel D, Buergler BE, Jud E, Muecke UP, Prestat M, Rupp JL, Richter J (2004) Solid oxide fuel cells: systems and materials. CHIMIA Int J Chem 58:837–850. https://doi.org/10.2533/000942904777677047
30. Buyukaksoy A, Birss VI (2016) Highly active nanoscale Ni - Yttria stabilized zirconia anodes for micro-solid oxide fuel cell applications. J Power Sources 307:449–453. https://doi.org/10.1016/j.jpowsour.2015.12.022
31. Ralph JM, Cécile R, Kumar R (2003) Cathode materials for reduced-temperature SOFCs. J Electrochem Soc. https://doi.org/10.1149/1.1617300
32. Plonczak P, Søgaard M, Bieberle-Hütter A, Hendriksen PV, Gauckler LJ (2012) Electrochemical characterization of La0.58Sr0.4Co0.2Fe0.8O3−δ thin films electrodes prepared by pulsed laser deposition. J Electrochem Soc 159:B471. https://doi.org/10.1149/2.100205jes
33. Lee J-W, Liu Z, Yang L, Abernathy H, Choi S-H, Kim H-E, Liu M (2009) Preparation of dense and uniform La0.6Sr0.4Co0.2Fe0.8O3−δ (LSCF) films for fundamental studies of SOFC cathodes. J Power Sources 190:307–310. https://doi.org/10.1016/j.jpowsour.2009.01.090
34. Beckel D, Muecke U, Gyger T, Florey G, Infortuna A, Gauckler L (2007) Electrochemical performance of LSCF based thin film cathodes prepared by spray pyrolysis. Solid State Ionics 178:407–415. https://doi.org/10.1016/j.ssi.2007.01.019
35. Angoua BF, Slamovich EB (2012) Single solution spray pyrolysis of La0.6Sr0.4Co0.2Fe0.8O3−δ–Ce0.8Gd0.2O1.9 (LSCF–CGO) thin film cathodes. Solid State Ionics 212:10–17. https://doi.org/10.1016/j.ssi.2012.02.015
36. Celikbilek Ö, Jauffrès D, Siebert E, Dessemond L, Burriel M, Martin CL, Djurado E (2016) Rational design of hierarchically nanostructured electrodes for solid oxide fuel cells. J Power Sources 333:72–82. https://doi.org/10.1016/j.jpowsour.2016.09.156
37. Marinha D, Dessemond L, Djurado E (2012) Electrochemical investigation of oxygen reduction reaction on La0.6Sr0.4Co0.2Fe0.8O3−δ cathodes deposited by electrostatic spray deposition. J Power Sources 197:80–87. https://doi.org/10.1016/j.jpowsour.2011.09.049
38. Celikbilek O, Jauffres D, Dessemond L, Burriel M, Martin CL, Djurado E (2016) A Coupled experimental/numerical approach for tuning high-performing SOFC-Cathode. ECS Trans 72:81–92. https://doi.org/10.1149/07207.0081ecst
39. Prestat M, Koenig J-F, Gauckler LJ (2007) Oxygen reduction at thin dense La0.52Sr0.48Co0.18Fe0.82O3–δ electrodes. J Electroceram 18:87–101. https://doi.org/10.1007/s10832-007-9012-y
40. Prestat M, Infortuna A, Korrodi S, Rey-Mermet S, Muralt P, Gauckler LJ (2007) Oxygen reduction at thin dense La0.52Sr0.48Co0.18Fe0.82O3–δ electrodes. J Electroceram 18:111–120. https://doi.org/10.1007/s10832-007-9021-x
41. Anderson H. U., C. C. Chen and M. M. Nasrallah, U. S. Patent No.5, 494, 700, Feb. 1996.
42. Buyukaksoy A, Kammampata SP, Birss VI (2015) Effect of porous YSZ scaffold microstructure on the long-term performance of infiltrated Ni-YSZ anodes. J Power Sources 287:349–358. https://doi.org/10.1016/j.jpowsour.2015.04.072
43. Darbandi AJ, Hahn H (2009) Nanoparticulate cathode thin films with high electrochemical activity for low temperature SOFC applications. Solid State Ionics 180:1379–1387. https://doi.org/10.1016/j.ssi.2009.07.010
44. Mineshige A, Izutsu J, Nakamura M, Nigaki K, Abe J, Kobune M, Fujii S, Yazawa T (2005) Introduction of A-site deficiency into La0.6Sr0.4Co0.2Fe0.8O3–δ and its effect on structure and conductivity. Solid State Ionics 176:1145–1149. https://doi.org/10.1016/j.ssi.2004.11.021
45. Zhou W, Ran R, Shao Z, Zhuang W, Jia J, Gu H, Jin W, Xu N (2008) Barium- and strontium-enriched (Ba0.5Sr0.5)1 xCo0.8Fe0.2O3−δ oxides as high-performance cathodes for intermediate-temperature solid-oxide fuel cells. Acta Mater 56:2687–2698. https://doi.org/10.1016/j.actamat.2008.02.002
46. Gordes P, Christiansen N, Jensen EJ, Villadsen J (1995) Synthesis of perovskite-type compounds by drip pyrolysis. J Mater Sci 30:1053–1058. https://doi.org/10.1007/bf01178444
47. Angoua BF, Cantwell PR, Stach EA, Slamovich EB (2011) Crystallization and electrochemical performance of La0.6Sr0.4Co0.2Fe0.8O3−δ-Ce0.8Gd0.2O1.9 thin film cathodes processed by single solution spray pyrolysis. Solid State Ionics 203:62–68. https://doi.org/10.1016/j.ssi.2011.08.017
48. Molero-Sánchez B, Addo P, Buyukaksoy A, Birss V (2017) Performance enhancement of La0.3Ca0.7Fe0.7Cr0.3O3-δAir electrodes by infiltration methods. J Electrochem Soc. https://doi.org/10.1149/2.0151710jes
49. Molero-Sánchez B, Addo P, Buyukaksoy A, Paulson S, Birss V (2015) Electrochemistry of La0.3Sr0.7Fe0.7Cr0.3O3−δ as an oxygen and fuel electrode for RSOFCs. Faraday Discuss 182:159–175. https://doi.org/10.1039/c5fd00029g
50. Reddy KR, Karan K (2005) Sinterability, mechanical, microstructural, and electrical properties of gadolinium-doped ceria electrolyte for low-temperature solid oxide fuel cells. J Electroceram 15:45–56. https://doi.org/10.1007/s10832-005-1099-4
51. Simner SP, Anderson MD, Engelhard MH, Stevenson JW (2006) Degradation Mechanisms of La–Sr–Co–Fe–O_3 SOFC Cathodes. Electrochem Solid-State Lett. https://doi.org/10.1149/1.2266160

52. Vovk G, Chen X, Mims CA (2005) In situ XPS studies of perovskite oxide surfaces under electrochemical polarization. J Phys Chem B 109:2445–2454. https://doi.org/10.1021/jp0486494
53. Lee W, Yildiz B (2013) Factors that influence cation segregation at the surfaces of perovskite oxides. ECS Trans 57:2115–2123. https://doi.org/10.1149/05701.2115ecst
54. Cai Z, Kubicek M, Fleig J, Yildiz B (2012) Chemical heterogeneities on La0.6Sr0.4CoO3−δ thin films—correlations to cathode surface activity and stability. Chem Mater 24:1116–1127. https://doi.org/10.1021/cm203501u
55. Lee W, Han JW, Chen Y, Cai Z, Yildiz B (2013) Cation size mismatch and charge interactions drive dopant segregation at the surfaces of manganite perovskites. J Am Chem Soc 135:7909–7925. https://doi.org/10.1021/ja3125349
56. Liu Y, Chen J, Wang F, Chi B, Pu J, Jian L (2014) Performance stability of impregnated La0.6Sr0.4Co0.2Fe0.8O3−δ–Y2O3 stabilized ZrO2 cathodes of intermediate temperature solid oxide fuel cells. Int J Hydrog Energy 39:3404–3411. https://doi.org/10.1016/j.ijhydene.2013.12.073
57. Dieterle L, Bockstaller P, Gerthsen D, Hayd J, Ivers-Tiffée E, Guntow U (2011) Microstructure of nanoscaled La0.6Sr0.4CoO3-δ cathodes for intermediate-temperature solid oxide fuel cells. Adv Energy Mater 1:249–258. https://doi.org/10.1002/aenm.201000036
58. Zhang T, Ma J, Kong L, Chan S, Hing P, Kilner JA (2004) Iron oxide as an effective sintering aid and a grain boundary scavenger for ceria-based electrolytes. Solid State Ionics 167:203–207. https://doi.org/10.1016/j.ssi.2004.01.006
59. Mazan MO, Marrero-Jerez J, Soldati A, Núñez P, Larrondo SA (2015) Fe-doped ceria nanopowders synthesized by freeze-drying precursor method for electrocatalytic applications. Int J Hydrog Energy 40:3981–3989. https://doi.org/10.1016/j.ijhydene.2015.01.006